MNRAS 518, 2661-2670 (2023) Advance Access publication 2022 November 4

# Precise near-infrared photometry, accounting for precipitable water vapour at SPECULOOS Southern Observatory

Peter P. Pedersen, 1\*† C. A. Murray, 1,2 D. Queloz, M. Gillon, B. O. Demory, A. H. M. J. Triaud, 5 J. de Wit, L. Delrez , 3,7 G. Dransfield , E. Ducrot, L. J. Garcia, Y. Gómez Magueo Chew, M. N. Günther, <sup>10</sup><sup>‡</sup> E. Jehin, <sup>7</sup> J. McCormac, <sup>11</sup> P. Niraula, <sup>6</sup> F. J. Pozuelos, <sup>3,7</sup> B. V. Rackham <sup>6</sup>, <sup>6,12</sup>§ N. Schanche, <sup>4</sup> D. Sebastian <sup>6</sup>, <sup>5</sup> S. J. Thompson, <sup>1</sup> M. Timmermans <sup>3</sup> and R. Wells <sup>4</sup>

Accepted 2022 October 27. Received 2022 October 26; in original form 2022 June 7

## **ABSTRACT**

The variability induced by precipitable water vapour (PWV) can heavily affect the accuracy of time-series photometric measurements gathered from the ground, especially in the near-infrared. We present here a novel method of modelling and mitigating this variability, as well as open-sourcing the developed tool - Umbrella. In this study, we evaluate the extent to which the photometry in three common bandpasses (r', i', z'), and SPECULOOS' primary bandpass (I + z'), are photometrically affected by PWV variability. In this selection of bandpasses, the I+z' bandpass was found to be most sensitive to PWV variability, followed by z', i', and r'. The correction was evaluated on global light curves of nearby late M- and L-type stars observed by SPECULOOS' Southern Observatory (SSO) with the I + z' bandpass, using PWV measurements from the LHATPRO and local temperature/humidity sensors. A median reduction in RMS of 1.1 per cent was observed for variability shorter than the expected transit duration for SSO's targets. On timescales longer than the expected transit duration, where long-term variability may be induced, a median reduction in RMS of 53.8 per cent was observed for the same method of correction.

**Key words:** atmospheric effects – techniques: photometric.

## 1 INTRODUCTION

Ground-based photometric observations are affected by atmospheric variability. A major source of this contamination comes from the multitude of molecular absorption lines which are known to affect atmospheric transmission. Predominantly in the nearinfrared, time-varying amounts of H2O in different layers of the atmosphere affect ground-based observations across a wide range of wavelengths - with the amount of H<sub>2</sub>O in a column of our atmosphere quantified as the amount of 'precipitable water vapour' (PWV), normally quoted in millimetres. O<sub>3</sub>, O<sub>2</sub>, CO<sub>2</sub>,

© 2022 The Author(s)

and CH<sub>4</sub>, amongst other molecular absorption lines, likewise play a role, however, often to a lesser extent (Smette et al. 2015).

To mitigate the majority of atmospheric effects, techniques such as differential photometry are commonly adopted (Howell 2006). They involve simultaneous observations of multiple objects in a field of view to estimate first-order changes of atmospheric transmission and instrumental effects over the course of an observational period. In differential photometry, objects of similar brightness and spectral energy distribution are used to calculate an 'artificial' comparison star. For example, in Murray et al. (2020), the artificial comparison star was created by applying a weight to all the objects in the field of view, accounting for their effective temperature, noise, variability, and distance to the target of interest. However, depending on the observational bandpass and an object's spectral energy distribution, the net flux observed on the ground can be seen to vary from object to object if the atmosphere is time-variable in its composition – leading

<sup>&</sup>lt;sup>1</sup>Cavendish Laboratory, JJ Thomson Avenue, Cambridge CB3 0HE, UK

<sup>&</sup>lt;sup>2</sup>Department of Astrophysical and Planetary Sciences, University of Colorado Boulder, 2000 Colorado Ave, Boulder, CO 80309, USA

<sup>&</sup>lt;sup>3</sup>Astrobiology Research Unit, University of Liège, Allée du 6 août, 19, B-4000 Liège (Sart-Timan), Belgium

<sup>&</sup>lt;sup>4</sup>University of Bern, Center for Space and Habitability, Gesellschaftsstrasse 6, CH-3012 Bern, Switzerland

<sup>&</sup>lt;sup>5</sup>School of Physics and Astronomy, University of Birmingham, Edgbaston, Birmingham B15 2TT, United Kingdom

<sup>&</sup>lt;sup>6</sup>Department of Earth, Atmospheric and Planetary Sciences, MIT, 77 Massachusetts Avenue, Cambridge, MA 02139, USA

<sup>&</sup>lt;sup>7</sup>Space sciences, Technologies and Astrophysics Research (STAR) Institute, University of Liège, Liège, B-4000, Belgium

<sup>&</sup>lt;sup>8</sup>AIM, CEA, CNRS, Université Paris-Saclay, Université de Paris, F-91191 Gif-sur-Yvette, France

<sup>9</sup> Instituto de Astronomía, Universidad Nacional Autónoma de México, Ciudad Universitaria, Ciudad de México, 04510, México

<sup>&</sup>lt;sup>10</sup>European Space Agency (ESA), European Space Research and Technology Centre (ESTEC), Keplerlaan 1, 2201 AZ Noordwijk, the Netherlands

<sup>&</sup>lt;sup>11</sup>Department of Physics, University of Warwick, Coventry CV4 7AL, UK

<sup>&</sup>lt;sup>12</sup>Department of Physics, and Kavli Institute for Astrophysics and Space Research, Massachusetts Institute of Technology, Cambridge, MA 02139, USA

<sup>\*</sup> E-mail: ppp25@cam.ac.uk

<sup>†</sup> Paris Region Fellow, Marie Sklodowska-Curie Action.

**<sup>±</sup> ESA** Research Fellow.

<sup>§ 51</sup> Pegasi b Fellow.

to a second-order differential effect which cannot be corrected by differential photometry.

This effect is a particularly significant problem for high-precision ground-based photometric studies of cool stars, such as M dwarfs and later types (e.g. Blake et al. 2008; Irwin et al. 2008; Tamburo et al. 2022). This is due to the large disparity in spectral energy distribution frequently observed in a field of view, as cool stars are typically much redder than the comparison stars suitable for differential photometry in any given field of view. To reduce this effect, one could observe with a narrow-band filter (e.g. Garcia-Mejia et al. 2020), but at the cost of instrumental precision due to the reduction in photons collected. Instead, most of these studies have relied on post-correction methods to reduce the nature of this effect, with varying degrees of success.

Irwin et al. (2011) developed a 'common mode' approach, which they applied to MEarth's northern survey (715 nm long-pass filter). This approach involved using median values over 30-min periods from multiple simultaneous observations of similar type objects, from 8 independent telescopes. The common mode, scaled per target via a least-squares optimization, was then used to correct for atmospheric effects over the course of a target's observation run. They noted that the scaling values correlated with stellar type.

Some observational bandpasses can be extremely sensitive to PWV changes, such as MEarth's bandpass and the primary bandpass used in this study (I + z', 700–1100 nm). Such bandpasses induce false variability, including structures able to mimic a transit feature or to hide a real one in differentially resolved light curves when subject to PWV changes over the course of an observation. To correct for this variability, atmospheric transmission profiles in the near-infrared can be modelled with tools such as Molecfit (Smette et al. 2015). These models can be used to correct photometric observations when the spectra of the observed objects are also known. Methods of quantifying PWV changes are therefore necessary for photometric surveys which use sensitive bandpasses, with temporal resolutions at least half the minimum expected transit duration to resolve such features, to follow Nyquist sampling.

In astronomy, on-site atmospheric transmission profiles are often inferred by spectrographs or by multiband photometers with strategically placed narrow-band filters. The aTmcam multiband instrument (Li et al. 2012, 2014) for instance, located on Cerro Tololo at  $\sim\!2200$  m, was able to quantify atmospheric PWV with a stated precision  $\sim\!0.6$  mm. A similar instrument called CAMAL (Baker, Blake & Sliski 2017), located on Mount Hopkins at  $\sim\!2600$  m (same site as MEarth's northern facility), had a stated precision of better than 0.5 mm in dry conditions (PWV < 4 mm). The use of a spectrograph on the other hand, such as in Li et al. (2017), gained a precision of 0.11 mm when evaluating high-resolution near-infrared H-band spectra of hot stars from the APOGEE spectrograph (located on the Apache Point Observatory at  $\sim\!2800$  m), calibrated with GPS-derived PWV values.

PWV values derived from timing delays in GPS signals have historically been used for meteorological studies, with large networks of GPS-PWV derived data in the public domain, such as the SuomiNet project (Ware et al. 2000) − typically with a precision of ∼1 mm. Remote-sensing satellites have likewise enabled wide spatial and temporal coverage of a multitude of atmospheric parameters globally. Marín, Pozo & Curé (2015) were able to estimate PWV in very dry conditions at the Chajnantor plateau (at ∼5100 m) with historical observations made by the now-decommissioned GOES-12 satellite and validated by an on-site radiometer. They attained absolute relative errors of 51 per cent and 33 per cent over the ranges 0−0.4 mm and 0.4−1.2 mm, respectively. Similar work was achieved

in Valdés, Morris & Demory (2021), yielding better uncertainties for Cerro Paranal at around 27 per cent, validated similarly with an on-site radiometer.

Radiometers derive PWV values from water vapour emission lines in the GHz region. At high altitudes, or low PWVs, the 183 GHz emission line is often observed. At the Paranal Observatory (with an elevation of  $\sim\!2600$  m), a 183 GHz based radiometer was commissioned in October 2011, the Low Humidity and Temperature Profiling microwave radiometer (LHATPRO; Kerber et al. 2012), located on the VLT platform. It has a quoted accuracy of better than 0.1 mm (when PWV between 0.5–9 mm) and a precision of 0.03 mm, with a saturation limit of 20 mm.

The motivation for this study derives from the SPECULOOS (Search for habitable Planets EClipsing ULtra-cOOl Stars; Gillon 2018; Delrez et al. 2018; Murray et al. 2020; Sebastian et al. 2020; Sebastian et al. 2020) project, a ground-based photometric survey targeting nearby (<40 pc) late M- and L-type stars, with its primary aim to discover transiting terrestrial planets. Exoplanets found with the SPECULOOS survey, like TRAPPIST-1 found by the SPECULOOS prototype survey (Gillon et al. 2017), will enable the unique opportunity to observe their atmospheres for potential biological signals with future large observatories. However, to maximize the probability of finding such planets, one must minimize the red noise the survey is subjected to, including the noise induced by atmospheric PWV variability.

In this work, we have developed methods to photometrically correct for PWV-induced variability on differential light curves. Our study has been evaluated on photometric data from SPECULOOS' Southern Observatory (SSO), which consists of four 1 m class telescopes located at the Paranal Observatory (Jehin et al. 2018). We utilized the standard observing modes of the LHATPRO instrument (located ~200 m above and a 1.8 km lateral distance away from SSO), in addition to ground relative humidity and temperature measurements. These measurements have been used to estimate the PWV experienced by SSO observations by including an altitude difference correction and line-of-sight estimate. We have also assessed the impact of photometric contamination by the temporally varying atmospheric PWV in several commonly used filter bandpasses, extending the work on the PWV correction described in Murray et al. (2020). In the following sections, we describe our methodology, quantify the extent of PWV variability at Paranal, its effect on common red-visible - near-infrared bandpasses, and evaluate our correction method on photometric observations from SSO performed with the I + z' bandpass.

# 2 METHOD OF CORRECTION

The observed flux of an object through our atmosphere can be described as

$$f(X, PWV, T_{eff}, t) = \int W(\lambda, X, PWV, t) R(\lambda) S(\lambda, T_{eff}, t) d\lambda,$$
 (1)

where  $W(\lambda, X, PWV, t)$  is the atmospheric transmission as function of wavelength  $(\lambda)$ , airmass (X), and PWV value with time (t).  $R(\lambda)$  is the overall bandpass response as a function of wavelength.  $S(\lambda, T_{\rm eff}, t)$  is the flux density distribution of an observed object as a function of wavelength, effective temperature  $(T_{\rm eff})$ , and time.

In Fig. 1, the amount with which different PWV values affect visible and near-infrared atmospheric transmission is shown. When equation (1) is applied, the change of flux as a function of PWV can be observed to differ significantly as a function of effective temperature; this is illustrated in Fig. 2 for the main bandpasses used by SPECULOOS (r', i', z', and I + z'). For differential photometry, a

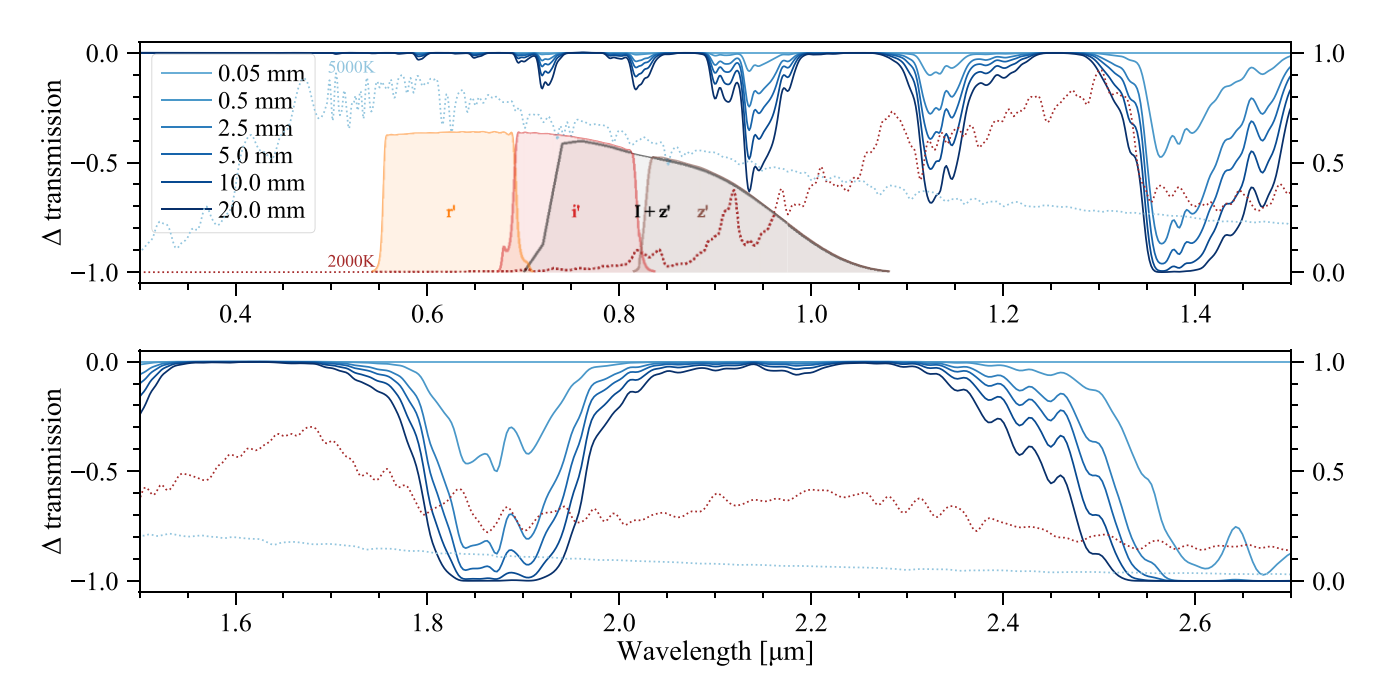


**Figure 1.** The fractional change of atmospheric transmission (left-hand axis) from the visible to near-infrared, at airmass 1, from a PWV of 0.05 to 20 mm is shown via a series of low resolution atmospheric spectra (from the SkyCalc Sky Model Calculator, for 2400 m; Jones et al. 2013; Noll et al. 2012). 5000 K and 2000 K stellar spectra are superimposed as dotted lines, from PHOENIX BT-Settl models (Allard, Homeier & Freytag 2012). Four observational bandpasses (right-hand axis), r', i', z', I + z', with instrumental efficiencies of a telescope equipped with a deeply depleted CCD accounted for are also shown.

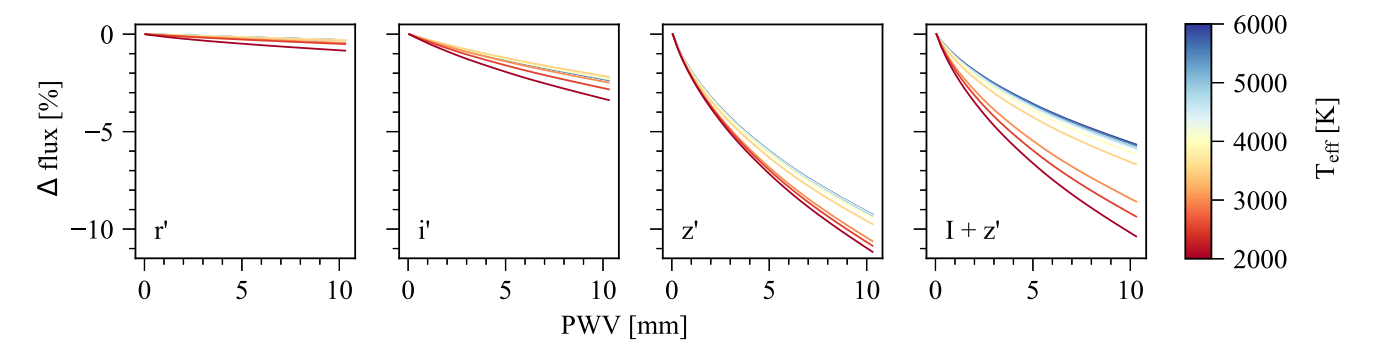


**Figure 2.** The change in flux as a function of PWV for different-temperature stars (from 6000 K to 2000 K in steps of 500 K) as modelled through four observational bandpasses, r', i', z', and I + z' (profiles shown in Fig. 1), with respect to a 0.05 mm PWV atmosphere at airmass 1.

second-order differential effect is thus induced when PWV is time-variable.

One can divide out this effect by modelling the expected differential light curve produced by PWV variability, as per equation (1). The difficulty in this approach stems from acquiring line-of-sight PWV values, in addition to having representative flux density distributions of the objects observed.

# 2.1 The PWV grid

For each filter bandpass, we have developed a grid which outputs a time-independent value from equation (1), when fed in observational parameters. These parameters are airmass (between 1 and 3), effective temperature (between 2000 and 36 500 K), and PWV (between 0.05 and 30 mm).

Each grid was built using atmospheric transmission profiles  $(0.5-2.0~\mu m)$  from the online SkyCalc Sky Model Calculator by ESO (Jones et al. 2013; Noll et al. 2012), for 2400 m (the closest available altitude to SPECULOOS' site, using the 'Entire year'

Entire night' profiles). In addition to these profiles, PHOENIX BT-Settl stellar models (Allard et al. 2012) provided by the Python Astrolib PySynphot Python package (Laidler et al. 2008) were used, with 2000 K as the lowest available temperature in the package. To build a stellar spectrum, one requires three parameters: effective temperature, metallicity, [Fe/H], and surface gravity, log(g). A representative set of stellar models were built using the parameters from Pecaut & Mamajek (2013), assigning a metallicity index of 0 to each spectra.

We generated 273 atmospheric profiles, a permutation of airmasses between 1 and 3 at 0.1 intervals, and PWV values between 0.05 and 30 mm ([0.05, 0.1, 0.25, 0.5, 1.0, 1.5, 2.5, 3.5, 5.0, 7.5, 10.0, 20.0, 30.0] mm). We then included a set of 91 stellar spectra to produce a grid of 24 843  $f(X, PWV, T_{eff}, t)$  values from equation (1) to interpolate

<sup>1</sup>Specifically, the updated values from https://www.pas.rochester.edu/~ema majek/EEM\_dwarf\_UBVIJHK\_colors\_Teff.txt version 2019.3.22, where the 1960 K effective temperature was rounded to 2000 K.

in between. We have made the PWV grid code, Umbrella, publicly accessible on GitHub.

### 2.2 PWV measurements - estimating line-of-sight PWV

We estimated line-of-sight PWV values by linearly interpolating over airmass between two measurements provided by the LHATPRO, one at zenith and another at an airmass of 2 (altitude of  $30^\circ$ ) from its cone scan measurements. Cone scan measurements were an average of four measurements at different bearings at a fixed altitude of  $30^\circ$ , with its value scaled by the LHATPRO service as if observed at zenith. Zenith and cone scan values were measured at  $\sim\!\!2$  and  $\sim\!\!15$  min cadences, respectively. The LHATPRO also produces an all-sky scan value every  $\sim\!\!6$  h, but these were not considered here.

LHATPRO PWV measurements, for the period of this study, were acquired via ESO's Ambient Query Form<sup>3</sup> in two stages. The first stage was acquired before the online archive was updated on 2020 Aug 28, the second stage was acquired after the update. Before the update, the data downloaded included zenith, cone scan, and all-sky measurements. Unfortunately for these measurements, a running average over five measurements and a  $\sim$ 1 min smoothing time-average was done by the service prior to downloading from the online archive. As a result, the different measurement types were not labelled or regularly spaced to be easily differentiable. To differentiate between the observing modes, we used a peak detection method. Large peaks spaced at  $\sim$ 6 h intervals (assumed to be all-sky measurements) were first removed, then peaks spaced at ~15 min intervals were registered as the average of 4 cone scan values and 1 zenith value. Thus, only cone scan measurements which were larger or equal to zenith measurements of this data set were subsequently identified.

The data acquired after the update only included zenith measurements, without the issue of the 5 point running average and the  $\sim$ 1 min time-average. The other measurement types were not made public at the time of acquisition. Thus, with the previously acquired data, and the new zenith values, we could estimate non-moving averaged cone scan measurements by using the new zenith measurements from around the same measurement period.

### 2.3 Accounting for altitude difference

The majority of water vapour resides close to the ground, with a scale height between 1 and 3 km (Kerber et al. 2017). The altitude difference of  $\sim\!200$  m between the LHATPRO at the VLT platform and SSO (located at the lower altitude) will therefore introduce an additional amount of PWV affecting our observations.

We estimated the missing vertical column of water vapour by integrating over the altitude difference,  $\Delta h$ , the estimated change in the density of water vapour,  $\rho$  (in kg m<sup>-3</sup>), between the respective sites,

$$PWV = \int \rho \, dh \approx \frac{1}{2} \Delta h \left( \rho_{\text{vlt}} + \rho_{\text{sso}} \right). \tag{2}$$

To estimate the PWV, a linear change in water vapour density was assumed between SSO,  $\rho_{sso}$ , and the VLT platform,  $\rho_{vlt}$ , where the LHATPRO is located. This yields a value in kg m<sup>-2</sup>, equivalent to PWV in millimetres when liquid density of water is 1000 kg m<sup>-3</sup>.

To estimate the density of water vapour (Sensirion 2009), one can use ambient temperature, T in  $^{\circ}$ C, and relative humidity, RH, measurements from the respective sites:

$$\rho = 0.2167 \text{ RH } \frac{6.112 \exp\left(\frac{17.62 T}{243.12+T}\right)}{273.15 + T} f_w(P), \tag{3}$$

where  $f_w(P)$  is 'water vapour enhancement factor' as a function of pressure, P, in hPa:

$$f_w(P) = 1.0016 + 3.15 \times 10^{-6} P - 0.074 P^{-1},$$
 (4)

where pressure was assumed fixed over time for the respective altitudes.

We used existing temperature and humidity sensors from the respective sites to produce density estimates. At SSO, we used the temperature and relative humidity sensor (Sensirion SHT15) on board a Boltwood Cloud Sensor II, with an assumed accuracy of  $\pm 1^{\circ}\text{C}$  and  $\pm 4$  per cent on relative humidity. At the VLT platform, values of temperature and relative humidity were measured by a VAISALA METEOrological station 2 m above the platform, with a quoted accuracy of  $\pm 0.2\,^{\circ}\text{C}$  and  $\pm 1$  per cent, respectively (Sandrock, Amestica & Sarazin 1999).

The altitude difference was determined using Google Maps Elevation service (Google 2022), with LHATPRO's position on the VLT platform returning an altitude of 2633 m and SSO an altitude of 2446 m. For comparison, the altitude of VISTA's platform from Google Maps Elevation service was found to agree with ESO's stated value within 2 m. GPS-derived altitude values are also available at SSO, yielding a median value of 2482 m. The neighbouring facility to SSO, NGTS has a quoted altitude of 2440 m (Wheatley et al. 2018), which led us to disregard the GPS-derived value. It was decided to use the altitude difference given by Google Maps Elevation service of 187 m, with an assumed error of  $\pm 10$  m. The lateral distance between the LHATPRO and SSO of 1.8 km was ignored.

### 3 RESULTS AND DISCUSSION

The following sections detail the results of applying the PWV correction to differential light curves observed by SSO over the course of approximately 1 yr (2019 Feb 17–2020 Jan 31).

# 3.1 PWV variability at Paranal

We experienced a median zenith value of 2.3 mm, a median cone scan value of 2.9 mm (pre-scaled by the LHATPRO service, as if observed at zenith), and a median PWV value of 0.26 mm calculated from the altitude difference, throughout our nightly observations.

During our study, we assessed the absolute difference between  $30^\circ$  (airmass 2) cone scan values and zenith values, as shown in Fig. 3. We found a median percentage difference of 26 per cent, as shown by the 0.5 CDF mark on Fig. 3. However, since the detected cone scan PWV values were always to be higher than the zenith PWV values (due to the peak detection method described in Section 2.2), there is a possibility that the cone scan values are over reported in some instances. And as such, the PWV variation presented in Fig. 3 may be different in reality.

A similar difference was observed in further detail in Querel & Kerber (2014), where they analysed 21 months of periodic all-sky scans, performed by the LHATPRO every 6 h. From their study,

<sup>&</sup>lt;sup>2</sup>https://github.com/ppp-one/umbrella

<sup>&</sup>lt;sup>3</sup>https://archive.eso.org/wdb/wdb/asm/lhatpro\_paranal/form

<sup>&</sup>lt;sup>4</sup>Accuracy taken from the sensor's datasheet: https://sensirion.com/us/products/catalog/SHT15/ for the low humidity conditions seen in Paranal, Chile.

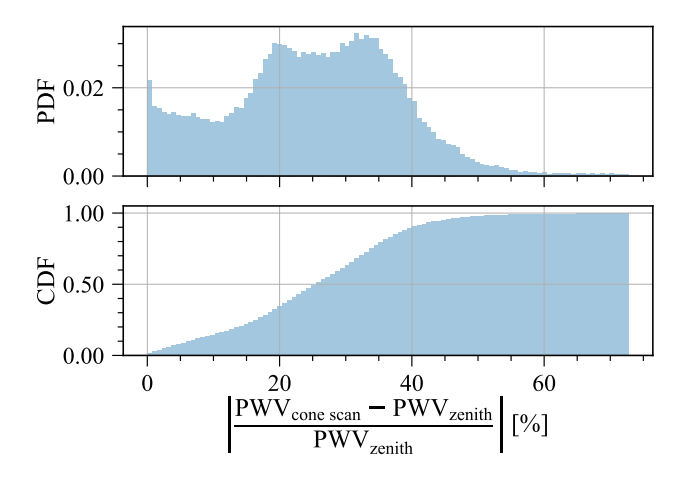


**Figure 3.** Probability density function (PDF) and cumulative distribution function (CDF) of the percentage difference between cone scan and zenith PWV measurements. Data from all publicly available nights, taking only dusk to dawn measurements.

they found a median all-sky variation of 10–26 per cent peak-to-valley, down to  $27.5^{\circ}$ , with respect to the all-sky's zenith value. From this, they argued that zenith observations of PWV are sufficient for the general analysis and correction of astronomical data at Paranal. However, with the increasing interest in cooler stars, photometric surveys may rely on line-of-sight PWV observations, depending on their desired photometric accuracy.

Fig. 4 and Table 1 detail the extent to which common near-infrared bandpasses (for silicon based detectors) will induce second-order differential variability with PWV changes experienced in Paranal during this study. Here, the respective change in a light curve's flux, per bandpass, of observing a late M-dwarf (with a temperature of 2700 K and a 5200 K comparison star - median temperatures of the sample in this paper) were simulated, using nightly PWV zenith data from the LHATPRO service. The I + z' bandpass was found to be the most sensitive to PWV variability, followed by z', i', and r'. On the hourly scale, the approximate expected transit duration for a temperate, rocky planet around a late-M or L-type star (Traub & Cutri 2008), the majority of PWV variability was found to induce a 0-1 mmag change in a light curve, within the typical photometric precision achieved by SSO. However, with z', and more significantly with the I + z' bandpass, changes greater than 1 mmag were observed at 16 per cent and 37 per cent occurrence rates respectively, mimicking transit structures from time to time.

The accuracy on  $\Delta$ PWV was calculated to be 0.042 mm, propagated from LHATPRO's stated single-measurement precision of 0.03 mm, assuming the accuracy of better than 0.1 mm of a single measurement to be systematic. For the I+z' bandpass, this accuracy level limits the correction to 0.4 mmag when PWV<sub>min</sub> is at 0.05 mm (the lower limit of the atmospheric models used), 0.2 mmag at Paranal's median value of 2.3 mm, and 0.1 mmag at a rarely seen 10 mm. This therefore suggests PWV measurements from the LHATPRO PWV measurement are sufficient for correcting submmag-level changes in our I+z' light curves, and even more so in the other band passes considered here.

The proportion of transit-like structures induced by zenith PWV variability over the evaluated data set was estimated in Table 2, using the same data as Table 1. This was calculated by finding the proportion of consecutive hours that displayed a dip in one hour and followed an equivalent rise, within  $\pm 25$  per cent, in the following hour. This method may miss some structures that occurred within

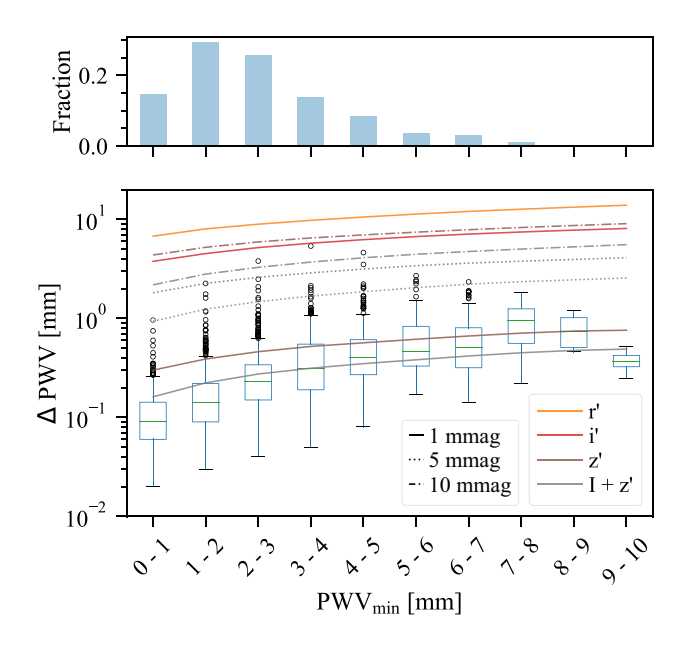


**Figure 4.** Sensitivity of common bandpasses and the I + z' bandpass to PWV changes. Bottom: Measured PWV changes from evaluated consecutive blocks of one hour intervals of PWV zenith data (only between the hours of dusk to dawn). Here, we calculated the max-min change ( $\Delta PWV$ ) of PWV within each evaluated hour. We grouped the measured changes into 1 mm intervals of PWV<sub>min</sub>, and plotted the respective box plots of the PWV changes from PWV<sub>min</sub> in each interval, where each box plot shows the standard median (green line), inter quartile range (IQR) of the lower (Q1) and upper (Q3) quartiles, and lower whisker (Q1 − 1.5\*IQR) and upper whisker lines (Q3 + 1.5\*IQR), with black circles denoting outliers of the whisker range. The coloured lines show the required  $\Delta PWV$  from the middle of each interval to induce a 1, 5, and 10 mmag change in a light curve (when observing a 2700 K target star and a 5200 K comparison star), represented by the solid, dotted, and dash-dotted lines, respectively, for each r', i', z', and I + z' bandpasses, in orange, red, brown, and grey, respectively. Changes at 5 and 10 mmag for r' and i' were outside the model's PWV range of 30 mm. Top: The fraction of hours contributing to the evaluated PWV interval ranges.

**Table 1.** Following Fig. 4, total proportion (in per cent) of consecutive blocks of one hour of PWV zenith data, only between the hours of dusk to dawn, which display a maximum change to a light curve's flux ( $\Delta$ LC) in mmag, per bandpass.

ΔLC (mmag)	$r^{'}$	i	z'	I + z
0–1	100.0	100.0	84.23	62.99
1–2	0.0	0.0	11.72	26.10
2-5	0.0	0.0	3.84	9.72
5-10	0.0	0.0	0.20	1.06
> 10	0.0	0.0	0.00	0.12

**Table 2.** Proportion (in per cent) of transit-like structures over the evaluated data set, within a range of depths in mmag, induced by PWV variability at zenith, per bandpass.

Depth (mmag)	$r^{'}$	$i^{'}$	z <sup>'</sup>	I+z	
0–1	10.17	10.17	8.71	6.35	
1-2	0.00	0.00	0.98	2.77	
2-5	0.00	0.00	0.49	0.90	
5-10	0.00	0.00	0.00	0.16	
> 10	0.00	0.00	0.00	0.00	

**Table 3.** Evaluation of the RMS percentage change,  $((\sigma_{LC \, corrected} - \sigma_{LC})/\sigma_{LC}) \times 100$ , of 103 global light curves (LC) with low and high pass filtering at 120 min. Showing the [10,25,50,75,90]th percentiles using the respective PWV derived values for correction, from zenith, zenith + altitude difference ( $\Delta$ Alt), estimated line of sight (Est. LoS), and Est. LoS +  $\Delta$ Alt.

	Low pass (per cent)			High pass (per cent)				
Percentiles (per cent)	Zenith	Zenith $+ \Delta Alt$	Est. LoS	Est. LoS $+ \Delta Alt$	Zenith	Zenith $+ \Delta Alt$	Est. LoS	Est. LoS $+ \Delta Alt$
10	-0.2	-0.2	-0.5	-0.1	1.7	1.7	4.3	4.0
25	-14.4	-14.4	-14.3	-16.0	0.2	0.2	0.4	0.5
50	-51.8	-52.9	-52.7	-53.8	-1.2	-1.3	-1.2	-1.1
75	-63.8	-64.5	-65.6	-66.2	-4.3	-4.3	-4.0	-3.9
90	-71.9	-72.1	-73.0	-73.5	-9.1	-8.6	-6.6	-6.1

an evaluated hour. None the less, it suggests the occurrence rate of a significant transit-like structure, greater than  $\sim$ 5 mmag, will not occur for the r' and i' bandpasses, and is a rare occurrence for both the z' and I+z' bandpasses. The I+z' bandpass will display a greater depth, given it has approximately twice the sensitivity to PWV changes than the z' bandpass when observing late M and L-type stars. If such an event occurs, it is likely to be visible in co-current observations of similar temperature targets by other telescopes on site in the same bandpass, if they exist.

SSO is subject to additional PWV-induced effects due to the altitude difference and observing through a variety of airmasses. The additional previously unaccounted for PWV from the altitude difference between SSO and the LHATPRO, calculated with the method described in Section 2.3, was seen to generally scale with zenith PWV, however was not seen to have a direct relationship with zenith values. The derived altitude difference PWV values were dependent on the accuracies of the respective temperature and humidity sensors, and the accuracy of the altitude difference in meters. Propagating the quantified errors on the derived altitude difference PWV data set provided a median fractional error of 18 per cent. The fractional error is likely higher in reality due to the approximation made in equation (2). The effect of the altitude derived PWV is evaluated in the following sub-section.

Similarly, the validity of linearly interpolating cone scan values over time, as described in Section 2.2, from a 15 min to a 2 min time base (to match the cadence of zenith measurements), was assumed to be acceptable. To test this assumption, we used the  $\sim$ 2 min cadence zenith values, and every 7th value from the data set linearly interpolated back onto the same time base as the original zenith observations, to simulate the cadence of the cone scan measurements. The difference between the values were found to be within  $\pm$ 2 per cent, under 0.1 mm in most cases. The validity of interpolating between zenith and cone scan values over airmass is addressed in the following sub-section.

### 3.2 Evaluation of the PWV correction

We used observations made by SSO with its primary bandpass, I + z'. SSO, with its four telescopes, made 1193 unique observations (divided by telescope/target/night) of 103 targets observed between 2019 Feb 17 to 2020 Jan 31 with the I + z' bandpass. This amounted to a sum of 5420 h of on-sky data. Differential light curves of these observations were produced with the SSO pipeline described in Murray et al. (2020).

For the correction, the target star was assigned an effective temperature derived in Sebastian et al. (2020), with an assumed systematic error of  $\pm 100$  K. The range of target temperatures evaluated was 2000–3000 K, with a median temperature of 2700 K.

The comparison light curve, behaving as an artificial star, had an effective temperature assigned by the SSO pipeline – a weighted sum of effective temperatures from the Gaia DR2 (Gaia Collaboration et al. 2018) catalogue, of the stars used in the field. The range of temperatures for the artificial star evaluated was 4000-6000 K, with a median temperature of 5200 K. For the I + z' bandpass, the secondorder effect induced by the artificial star behaves very similarly for any temperature above 4000 K, as illustrated in Fig. 2. The target star was often the coolest star in the field, and as such, forming an ideal artificial star with a temperature equivalent to the target star was not possible. Consequently, for the fields evaluated, this disparity in temperature between the target star and the effective comparison star would always yield a PWV induced effect under changing atmospheric conditions. One could potentially further improve the correction by fine-tuning the assigned effective temperature of the target, or by using the real spectra of the target - this was not considered here.

When searching for transits, we seek to minimize any atmospherically induced variability on differentially resolved light curves. This is to maximize the likelihood of detecting real transit events. In this context, the observed data set was evaluated in two regimes - with a low and high pass temporal filter, with a dividing period of 120 min. The low pass temporal filter maintained variability that was greater than 120 min, and high pass filter maintained the variability shorter than 120 min. This was to demonstrate the correction's effect around and below the transit time-scale, and on time-scales where longterm variability may be induced. Table 3 details the effectiveness of the correction. Here, we evaluated the percentage change in the root-mean-square (RMS) on global light curves (30 min binned) observed by SSO before and after the correction for the low and high pass temporally filtered domains. The correction was calculated with combinations of each of the PWV derived values (zenith, estimated line-of-sight, and altitude difference).

On time-scales longer than 120 min, a zenith PWV based correction demonstrated a large median RMS percentage change of -51.8 per cent, when compared to an uncorrected differential light curve. This large percentage change in RMS is attributed to the long-term multimillimetre variability of PWV, and as such demonstrates the correction's importance for variability studies on late-M and L-type stars, when using a bandpass like  $I+z^{'}$ . The addition of the altitude difference derived PWV to both zenith and estimated line-of-sight PWV made a marginal improvement, at -52.9 and -53.8 per cent, respectively. Using the estimated line-of-sight PWV alone yielded -52.7 per cent.

Whilst the estimated line-of-sight PWV presented a marginally better median percentage change, the assumption of circular symmetry around zenith in some instances may introduce false variability post-correction. To yield a more accurate correction, a new measurement mode for the LHATPRO is subsequently suggested: a

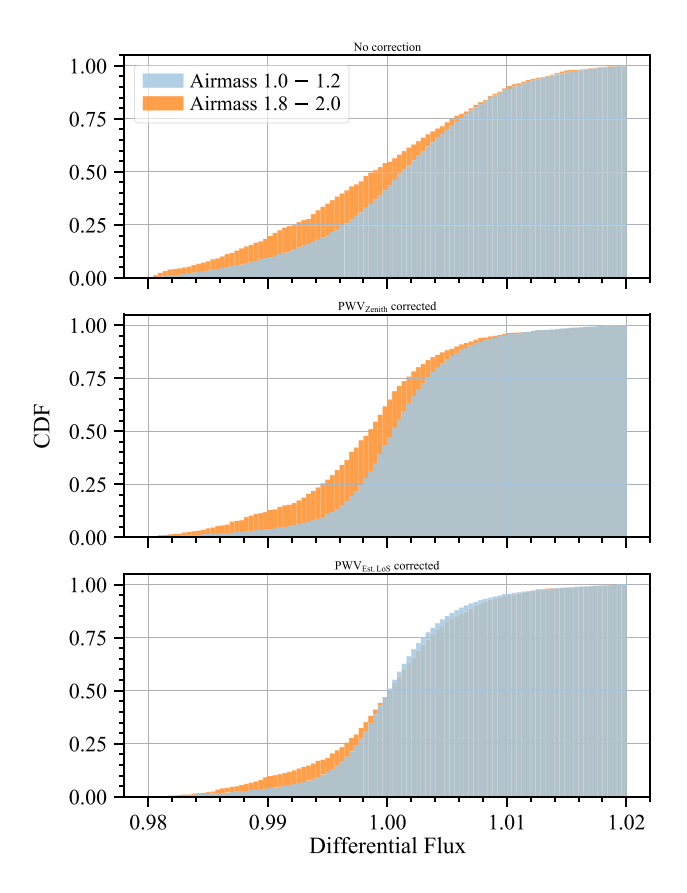


**Figure 5.** Assessing the correction's effect on differential flux at different airmass ranges. Cumulative distribution function (CDF) histograms of differential flux between 0.98 and 1.02 (of 0.005 JD binned on-sky data) observed with the  $I+z^{'}$  bandpass. Global data set assessed for when observations were in two different ranges of airmasses 1.0–1.2 and 1.8–2.0, with different levels of PWV derived corrections applied. First without any correction (top plot), zenith PWV correction (middle plot), and then estimated line-of-sight (Est. LoS) PWV correction (bottom plot).

continuous monitoring mode which constructs a low resolution all-sky map, maintaining a PWV accuracy of 0.1 mm, at a cadence better than 30 min (half the expected transit duration around a late M, L-type star, to follow Nyquist sampling). Since we only seek to minimize long-term variability and false transit features, the current 2 min cadence for zenith is faster than we currently need.

The estimated line-of-sight PWV also minimized a previously uncorrected airmass effect: an observed decrease of differential flux when transitioning to higher airmasses. This effect is illustrated in Fig. 5. Without the correction, a -3.0 mmag differential flux change from the median differential flux at airmasses between 1.0 and 1.2 to the median differential flux at airmasses between 1.8 and 2.0 was observed. This change improves slightly with the correction derived with zenith PWV, and noticeably improves with the estimated lineof-site PWV with a median differential flux increase of 0.1 mmag observed from airmasses between 1.0 and 1.2 to airmasses between 1.8 and 2.0, versus the -3.0 mmag observed without line-of-sight correction. We performed a two-sample Kolmogorov-Smirnov test to assess the statistical significance of this result, where we assessed the cumulative distributions of differential flux at high airmasses (1.8-2.0) corrected with zenith PWV values (Fig. 5, middle plot, orange CDF), F(x), to the correction derived from estimated line-ofsite PWV values (Fig. 5, bottom plot, orange CDF), G(x). Our null

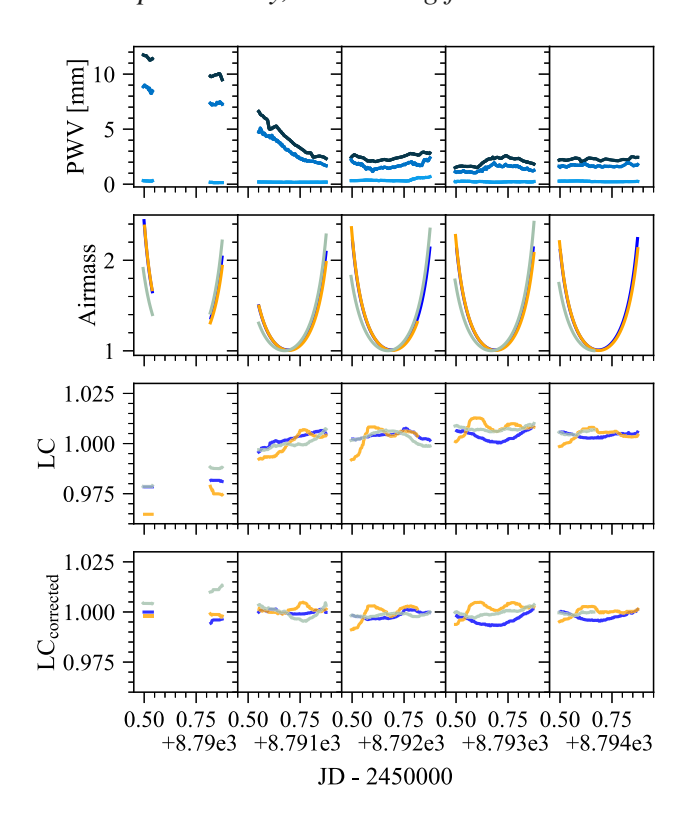


Figure 6. Five consecutive nights observed by three SSO telescopes of three different targets, one per telescope – distinguished by the different colours in the lower three plots. The first night is partially missing data due to bad weather. First row: PWV values from cone scan (dark blue), zenith (blue), altitude measurements (light blue) are shown. Second row: Airmass of the respective observations, which shows the transition between zenith and the airmass cone scan PWV measurements are made (airmass 2), used for the line-of-sight PWV estimate. Third row: Differential light curves (LC) without PWV correction. Bottom row: Differential light curves with PWV correction, using estimated line-of-sight + altitude difference PWV. The global light curves were normalized over the assessed period. The effective temperatures of the target/comparison stars were 2500/5000, in orange; 2600/4700, in light green; 2700/4300, in blue, respectively. The light curves shown are with a 120 min low pass filter applied – trends from 120 min windows using a median method. Here, the average 120 min binned error was sub-mmag for all light curves.

hypothesis being that  $F(x) \ge G(x)$  for all airmasses. The resulting Kolmogorov–Smirnov test yielded a p-value of 0.992, leading us to accept the null hypothesis, confirming our observation that line-of-sight PWV data helps to minimize the decreasing of differential flux at higher airmasses. From the distributions seen in Fig. 5, we can also see the reduced spread of differential flux when the correction is applied, as quantified in Table 3.

On time-scales shorter than 120 min, a median RMS percentage change of around -1 per cent for all PWV-derived values was observed. However, without the ground-truth of stellar variability at this scale, it's difficult to argue if one PWV derived correction is better than another when solely based on the RMS percentage change. While it has been seen to correct transit-like features in Murray et al. (2020) and one example in the next subsection, the correction at shorter time-scales was seen to increase the RMS in about a quarter of the instances evaluated. Once again, without the ground truth at this scale, or extended trend modelling, it's currently difficult to validate the true extent of improvement at this scale. It is therefore recommended to manually vet where possible. None the less, with

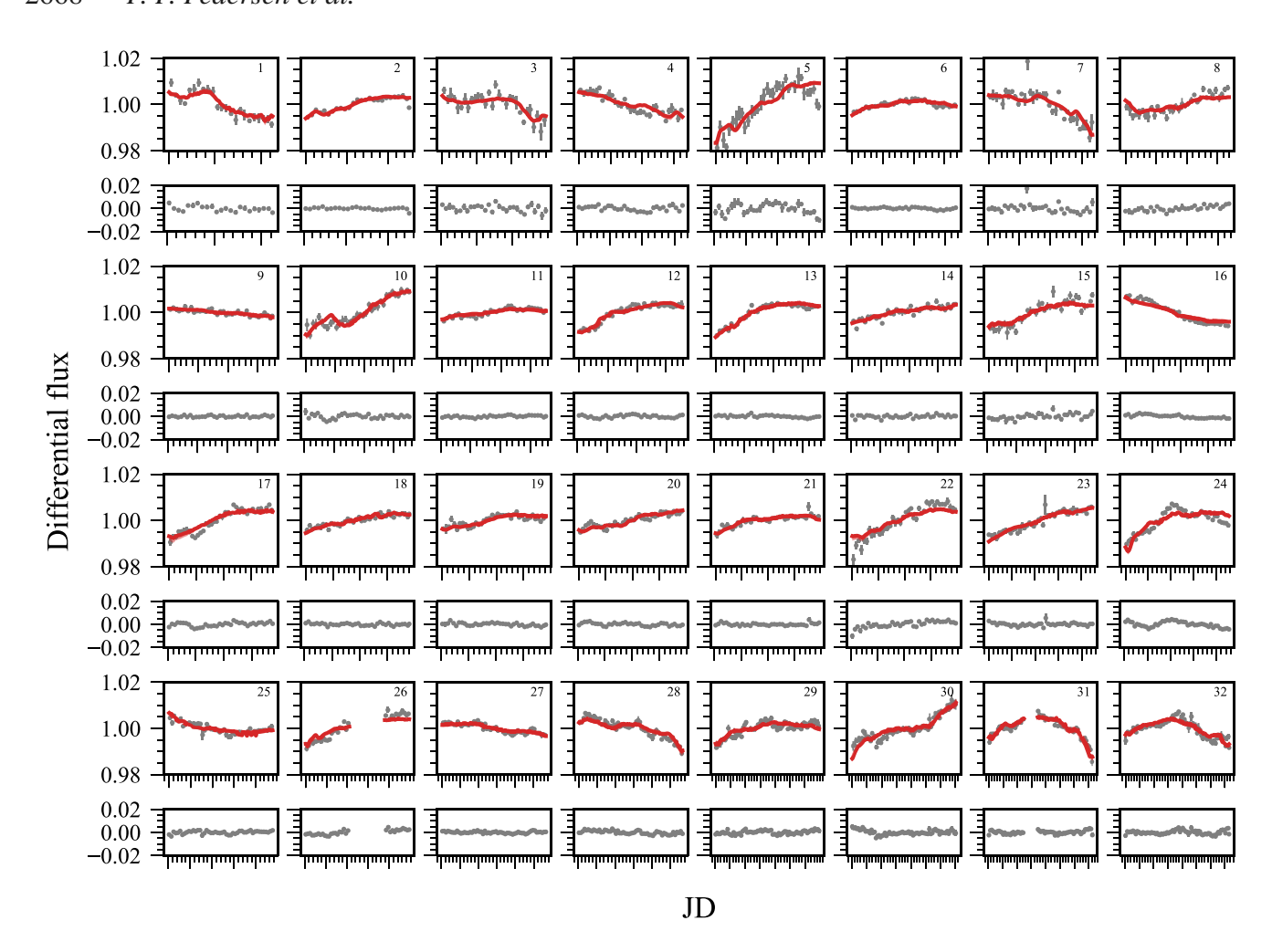


Figure 7. A selection of 32 observations of 19 different targets observed with the I + z' bandpass which matched closely with the expected trend from the correction. Top row: 0.005 JD binned (7.2 min) uncorrected differential flux light curves in grey. Expected trend from the correction in red, using estimated line-of-sight + altitude difference PWV and knowledge of the target and comparison stars effective temperatures. In shaded red, although the effect is not visible for the majority of examples, the expected trend from the correction also plotted using  $\pm 100 \, \text{K}$  from the target's effective temperature. Second row: Residual of the correction (observed data – expected trend) of the above subplot. Row order then repeats. Ordered from shortest to longest time-scales, where the major ticks on the x-axis are 0.05 JD (72 min).

the data set evaluated here, we have not seen instances where the correction has induced significant false variability. The cases where this may occur would be likely due to PWV measurement failure, or significant line-of-sight differences from observation and PWV measurement.

### 3.3 PWV correction in action

In this subsection, examples of the correction with the  $I+z^{'}$  bandpass are shown on the global and nightly scale. The first example, in Fig. 6, shows five consecutive nights of observations of three targets of similar temperature (2500–2700 K), with the global light curves normalized over the assessed period and with a 120 min low-pass filter applied. Between the first and second night, a large PWV change was observed. The resulting second-order effect is evident in the uncorrected light curves, showing around a 30 mmag change for all the targets. The behaviour on shorter timescales, however, was not always comparable between targets due to the respective variability that is often seen with M dwarfs (Günther et al. 2022). Beyond the

second night on Fig. 6, the PWV changes were less significant on the light curves by eye. However, a level of difference is still visible. No other systematic effects were seen to correlate with the observations.

The respective PWV values from zenith and cone scan followed a similar trend for the five nights. A similar PWV zenith and cone scan behaviour was seen for the remaining data set. The altitude difference derived PWV stayed relatively constant with the exception of the third night, where a small increase was observed at the end of the night, with an opposing change seen at zenith around the same time. A layer of water vapour likely transitioned from above the LHATPRO to the layers below it. A sharp dip in flux in all the light curves was observed at the same time. The correction removed the majority of the structure; however, some residual in the shape was left in all the light curves, suggesting some amount of water vapour was unaccounted for in the line-of-sight and altitude estimates. The residual shape could likewise be attributed to inaccuracies in the target and comparison stars temperature estimates, where a higher target temperature estimate would have under corrected the variability. This could be similarly argued for the light green target between the first and second nights. Co-current

observations of this target could not be found to rule out stellar variability.

If one were to adopt the methodology in Irwin et al. (2011), briefly described in Section 1, for time-scales greater than 120 min at 30 min bins, one would need at least nine co-current observations of similar temperature objects to yield a common mode with variability at the sub-mmag scale. At time-scales below 120 min, however, one would need an unrealistic 90 co-current observations. This was calculated by evaluating the overall RMS SSO experienced (with correction) at the respective scales, and assuming a RMS scaling of root sum the total number of co-current observations.

In Fig. 7, 32 examples of single observations are shown. In these examples, the uncorrected differential light curves displayed a close resemblance to the expected trend modelled by the PWV grid, with PWV values from the estimated line-of-sight and altitude difference. These were found by finding the nights where the standard deviation of the night's data was significantly reduced by the correction. Such examples often occur on quiet targets, where the second-order effects are very evident on both short and long time-scales. For example, on the shorter time-scales, false transit features have been mostly corrected for in subplots labelled 1, 3, and 12. On the longer timescales, a range of other variabilities are closely matched, such as an inverse airmass like shape in the subplot labelled 31. There is an instance in Fig. 7 where a transit like feature is induced by the correction (subplot labelled 10). The exact origin of this feature is unknown, most likely a line-of-sight induced feature. Manual vetting is therefore recommended when such events occur. The remaining light curves matched closely the expected trend modelled by the PWV grid, with many examples beyond the 32 presented light curves which similarly match the modelled trend.

### 4 CONCLUSIONS

We have developed a method of modelling and mitigating the second-order effect induced by PWV on time-series photometric data. This has been enabled by leveraging the accurate measurement modes provided by an onsite radiometer, the LHATPRO, and local environmental sensor data. The developed tool, the PWV grid, has proven to be an essential for SSO, and we believe it can help other studies who are likewise sensitive to PWV and have access to accurate PWV data. The PWV grid code, Umbrella, has been open-sourced on GitHub.<sup>5</sup>

We found, for removing transit-like structures and long term variability on late M- and early L-type stars, the LHATPRO's single measurement PWV accuracy of better than 0.1 mm, and precision of 0.03 mm, is sufficient to eliminate sub-mmag level PWV induced photometric effects for the  $I+z^{\prime}$  and  $z^{\prime}$  bandpasses, and more than sufficient for the  $i^{\prime}$  and  $r^{\prime}$  bandpass. The  $I+z^{\prime}$  bandpass was shown to be exceptionally sensitive to second-order effects induced by PWV, and without aid of the correction, the bandpass significantly limits ones ability to do variability studies on late M- and L-type stars. On the transit time-scale, the bandpass is sensitive to variability which may mimic transit-like structures on the rare occasion with Paranal's level of PWV variability.

PWV data from zenith was found to be sufficient to support the majority of the correction needed for the four telescopes at SSO. However, through our use of zenith and cone scan measurement modes, there are residual second-order effects induced at higher

airmasses which would require line-of-sight measurements to accurately correct for. We have therefore recommended a continuous all-sky observing mode for the LHATPRO, such to support more accurate line-of-sight estimates for our multiple telescopes at Paranal.

The additional PWV derived from the altitude difference between the LHATPRO and SSO was accounted for through the use of local environment sensors, and was shown to improve the correction on time-scales longer than 120 min. On shorter time-scales, a more accurate method of accounting for the altitude difference may be needed. If one does not have access to PWV data, then optimizing the bandpass for the survey is necessary.

#### **ACKNOWLEDGEMENTS**

The research leading to these results has received funding from the European Research Council (ERC) under the FP/2007–2013 ERC grant agreement no. 336480, and under the H2020 ERC grants agreements no. 679030 & 803193; and from an Actions de Recherche Concertée (ARC) grant, financed by the Wallonia-Brussels Federation. We also received funding from the Science and Technology Facilities Council (STFC; grants no. ST/S00193X/1, ST/00305/1, and ST/W000385/1). This work was also partially supported by a grant from the Simons Foundation (PI: Queloz, grant number 327127), as well as by the MERAC foundation (PI: Triaud), and the Balzan Prize foundation (PI: Gillon). PPP acknowledges funding by the Engineering and Physical Sciences Research Council Centre for Doctoral Training in Sensor Technologies and Applications (EP/L015889/1). ED acknowledges support from the innovation and research Horizon 2020 programme in the context of the Marie Sklodowska-Curie subvention 945298. MNG acknowledges support from the European Space Agency (ESA) as an ESA Research Fellow. This publication benefits from the support of the French Community of Belgium in the context of the FRIA Doctoral Grant awarded to MT. LD is an F.R.S.-FNRS Postdoctoral Researcher.

We would like to thank Alain Smette for his help and guidance with the LHATPRO data.

### DATA AVAILABILITY

The data underlying this article is not currently public. The SPECULOOS-South Consortium will make all SPECULOOS-South Facility reduced data products available to the ESO Science Archive Facility following the regular Phase 3 process as described at http://www.eso.org/sci/observing/phase3.html.

### REFERENCES

Allard F., Homeier D., Freytag B., 2012, Phil. Trans. Roy. Soc. London Ser. A, 370, 2765

Baker A. D., Blake C. H., Sliski D. H., 2017, PASP, 129, 085002

Blake C. H., Bloom J. S., Latham D. W., Szentgyorgyi A. H., Skrutskie M. F., Falco E. E., Starr D. S., 2008, PASP, 120, 860

Delrez L. et al., 2018, in Ground-based and Airborne Telescopes VII. p. 1070011

Gaia Collaboration et al., 2018, A&A, 616, A1

Garcia-Mejia J., Charbonneau D., Fabricant D., Irwin J., Fata R., Zajac J. M., Doherty P. E., 2020, in Ground-based and Airborne Telescopes VIII. p. 1387

Gillon M., 2018, Nature Astron., 2, 344

Gillon M. et al., 2017, Nature, 542, 456

Google, 2022, Google Maps Elevation API Digital Elevation Model. https://developers.google.com/maps/documentation/elevation/overview/Günther M. N. et al., 2022, AJ, 163, 144

<sup>&</sup>lt;sup>5</sup>https://github.com/ppp-one/umbrella

- Howell S. B., 2006, Handbook of CCD Astronomy, 2nd edn., Cambridge Observing Handbooks for Research Astronomers. Cambridge Univ. Press, Cambridge
- Irwin J., Charbonneau D., Nutzman P., Falco E., 2008, Proc. Int. Astr. Un., 4, 37
- Irwin J., Berta Z. K., Burke C. J., Charbonneau D., Nutzman P., West A. A., Falco E. E., 2011, ApJ, 727, 56
- Jehin E. et al., 2018, Messenger, 174, 2
- Jones A., Noll S., Kausch W., Szyszka C., Kimeswenger S., 2013, A&A, 560, A91
- Kerber F. et al., 2012, in Ground-based and Airborne Instrumentation for Astronomy IV. p. 84463N
- Kerber F., Querel R., Neureiter B., Hanuschik R., 2017, in ESO Calibration Workshop: The Second Generation VLT Instruments and Friends. p. 22
- Laidler V. G., Greenfield P., Busko I., Jedrzejewski R., 2008, in Proceedings of the 7th Python in Science Conference. p. 36
- Li T. et al., 2012, in Ground-based and Airborne Instrumentation for Astronomy IV. p. 84462L
- Li T., DePoy D., Marshall J. L., Nagasawa D., Carona D., Boada S., 2014, in Ground-based and Airborne Instrumentation for Astronomy V. p. 91476Z
- Li D., Blake C. H., Nidever D., Halverson S. P., 2017, PASP, 130, 014501 Marín J. C., Pozo D., Curé M., 2015, A&A, 573, A41
- Murray C. et al., 2020, MNRAS, 495, 2446

- Noll S., Kausch W., Barden M., Jones A. M., Szyszka C., Kimeswenger S., Vinther J., 2012, A&A, 543, A92
- Pecaut M. J., Mamajek E. E., 2013, ApJS, 208, 9
- Querel R. R., Kerber F., 2014, in Ramsay S. K., McLean I. S., Takami H., eds, Proc. SPIE Conf. Ser. Vol. 9147, Ground-based and Airborne Instrumentation for Astronomy V. SPIE, Bellingham, p. 914792,
- Sandrock S., Amestica R., Sarazin M., 1999, Doc no.: VLTMAN-ESO-17440-1773.
- Sebastian D. et al., 2020, in Ground-based and Airborne Telescopes VIII. p. 1144521
- Sebastian D. et al., 2020, preprint (arXiv:2011.02069)
- Sensirion, 2009, Introduction to Humidity: Basic Principles on Physics of Water Vapor. https://www.soselectronic.com/a\_info/resource/c/sensirion/Sensirion\_Introduction\_to\_Relative\_Humidity\_V2.pdf
- Smette A. et al., 2015, A&A, 576, A77
- Tamburo P. et al., 2022, preprint (arXiv:2201.01794)
- Traub W. A., Cutri R., 2008, in Fischer D., Rasio F. A., Thorsett S. E., Wolszczan A., eds, ASP Conf. Ser. Vol. 398, Extreme Solar Systems. Astron. Soc. Pac., San Francisco, p. 475
- Valdés E. M., Morris B., Demory B., 2021, A&A, 649
- Ware R. H. et al., 2000, Bull. Am. Meteorol. Soc., 81, 677
- Wheatley P. J. et al., 2018, MNRAS, 475, 4476

This paper has been typeset from a  $T_EX/I = T_EX$  file prepared by the author.